ISSN 0018-151X, High Temperature, 2020, Vol. 58, No. 4, pp. 632–646. © Pleiades Publishing, Ltd., 2020.
Russian Text © The Author(s), 2020, published in Teplofizika Vysokikh Temperatur, 2020, Vol. 58, No. 4, pp. 689–706.

HEAT AND MASS TRANSFER AND PHYSICAL GASDYNAMICS

Laser Ablation: Physical Concepts and Applications (Review)

N. A. Inogamov[a, b, *], **Yu. V. Petrov**[a, c], **V. A. Khokhlov**[a], **and V. V. Zhakhovskii**[b, d]

[a] *Landau Institute for Theoretical Physics, Russian Academy of Sciences, Chernogolovka, Moscow oblast,142432 Russia*
[b] *Dukhov Automatics Research Institute (VNIIA), Moscow, 127055 Russia*
[c] *Moscow Institute of Physics and Technology, Dolgoprudnyi, Moscow oblast, 141701 Russia*
[d] *Joint Institute for High Temperatures, Russian Academy of Sciences, Moscow, 125412 Russia*
**e-mail: nailinogamov@gmail.com*

Received March 16, 2020; revised March 26, 2020; accepted March 30, 2020

Abstract—Laser ablation (i.e., the removal of target material upon irradiation) is under consideration; it is widely applied in some technologies. Physical models needed for an understanding of ablation have been developed since the invention of the first lasers. Some phenomena have been thoroughly investigated; however, there are still many problems that should be analyzed additionally. These poorly studied phenomena include surface structuring. The problems concerning ablation in liquid and laser forging/peening are not yet completely understood. They represent two sides of the same process: in the first case, the emphasis is on the description of motion of the substance beyond the target, whereas, in the case of laser forging, one abstracts from the plume and considers the elastoplastic transformations caused by a shock wave inside a target. The hydrodynamics of these processes differs radically with the transition from ultrashort to long pulses.

DOI: 10.1134/S0018151X20040045

CONTENTS

INTRODUCTION

Three modern fields of the applications of laser systems are considered. The first is surface structuring, which changes the shape of an initially smooth surface of a target [1–16]. The morphology of the changes is diverse. The variety of geometric shapes is controlled with the laser-pulse parameters and the number of repetitions of pulses on a fixed point [1, 8, 17].

This technique is used to form metasurfaces, i.e., surfaces with artificially changed characteristics. The optical [2, 5, 13, 15, 18–21] and tribological characteristics and wettability are variable. Such surfaces cause sharp amplification of the Raman scattering [18, 19] and fluorescence [18, 19] of tested liquids deposited on the surface. This effect is used in highly sensitive sensors [18–21].

The second field is related to the formation of colloids during laser ablation in liquid (LAL) [19–38]. A colloid is a solution of nanoparticles. Nanoparticles are so small that they are able not to precipitate for years due to the viscous Stokes friction and Brownian motion. During the ablation of a target immersed in a transparent liquid (through which the target is irradiated), nanoparticles enter the liquid. Some of the material detaches from the target as nanoparticles during the ablation. The thus obtained colloids and nanoparticles are widely used in various applications (see the recent reviews on LAL [25, 26]).

Although experiments on nanoparticles, and their production, began more than twenty years ago, the physics of the phenomena underlying ablation in liquid became clearer only in recent years. The first quantitative studies were carried out at the Joint Institute for High Temperatures of the Russian Academy of Sciences [28, 29]. Those works studied ablation in vacuum and in water under irradiation by femtosecond pulses. It was assumed in the first qualitative studies that nanoparticles form due to the condensation of evaporated target material (as in the case of ablation in vacuum or air). However, it was revealed that the process is much more complex [23–40].

The third important field of science and technology is the laser hardening of materials (laser shock peening—LSP). The traditions of metal machining (forging/peening) go back to antiquity (e.g., the manufacture of damascus steels). The techniques of mechanical treatment known to date include the bom-

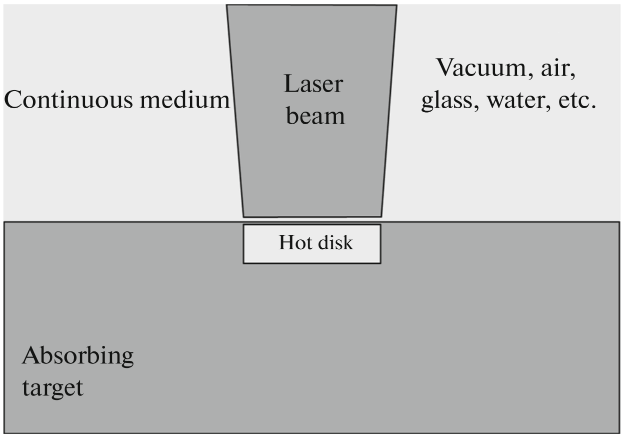

Fig. 1. Schematic of the studied laser irradiation.

bardment of products with a high-speed pellet flow, rolling, etc. Currently, laser irradiation is used instead of pellets [41–48]. The theoretical models of hardening have been insufficiently developed.

1. OBJECT OF STUDY AND SPECIFIC FEATURES OF FEMTOSECOND IRRADIATION

Figure 1 shows the studied situation. A laser beam passes through a transparent medium to a flat target surface. The transmission medium is vacuum, air, or transparent condensed matter (liquid or solid). The target is made of absorbing material (e.g., metal). Laser is a unique tool for energy transport focused in a specified region. In contrast to heat conduction (when a heat flux propagates in the material), this energy transfer is contactless. The problems of laser ablation compose a line of research related to thermal physics and mechanics. Both hydrodynamic phenomena and phenomena related to the mechanics of the deformed solid are important here.

In the early stages, a thin, hot disk forms under laser irradiation (Fig. 1). Its radial extension is determined by the radius R_L of the irradiation spot. The thermal disk thickness d_T varies from a score of nanometers to several micrometers. The thickness $d_T \approx 10$ nm is characteristic of low-conductivity metals (nickel, platinum, ruthenium, palladium, etc. [49–52]) and ultrashort laser pulses (USLPs) [53] (the USLP duration τ_L is from ~10 fs to several picoseconds). In the case of a long-term effect ($\tau_L = 1$–100 ns), the thickness d_T can be as large as several μm (at $\tau_L = 100$ ns) for high-conductivity metals (gold, silver, copper, and aluminum) [34].

Ultrashort Laser Pulses. Specificity of Two-Temperature States

In the two-temperature (2T) stage, the thermal conductivity of metals sharply increases [49–58] in comparison with the reference values corresponding to one-temperature (1T) states. In the 2T stage induced by USLPs, the electron temperature T_e is higher than the ion-subsystem temperature T_i. The 2T stage is of great importance in the case of the USLP, because a heating layer with a large thickness d_T forms in specifically this stage. The thickness d_T is generally equal to several skin-layer thicknesses δ_T: $\delta_T = 10$–20 nm in the case of metals and optical frequencies of electromagnetic radiation. The increase in metal thermal conductivity κ in the 2T stage is related to an increase in the electron specific heat C_e due to the partial removal of degeneracy [55]. The removal of degeneracy is, in turn, caused by intense heating of the electron subsystem to temperatures comparable to the Fermi temperature.

Let us clarify why the energy absorbed by electrons in the skin layer is transferred in a supersonic way from the skin layer in to the target bulk in the 2T stage. This effect is of fundamental importance. The supersonic formation of the heating layer d_T for USLPs qualitatively distinguishes the dynamics of ablation in this case from the flows of target material caused by long laser pulses.

According to the Drude model, the thermal conductivity κ can be estimated as $\kappa = (1/3)v_F^2 C_e/\nu_e$, where C_e is the specific heat of the electron subsystem per unit volume, v_F is the Fermi velocity, $\nu_e = 1/\tau_e$ is the electron collision frequency, and τ_e is the electron mean free time. With a partial removal of degeneracy, we have $C_e = \gamma T_e$. Within the Fermi gas approximation, factor γ is equal to $\gamma = \pi^2 n_e k_B^2/(2E_F)$, where n_e is the electron concentration in the conduction band, k_B is the Boltzmann constant, and E_F is the Fermi energy.

The frequency $\nu_e = \nu_{ei} + \nu_{ee}$ takes into account the interactions of an electron with ions and other electrons. The details of the thermal conductivity calculations were given in [59–65]. The situations in which the temperature is above the Debye temperature are of specific interest. When temperatures $T \sim T_i \sim T_e$ are below a temperature on the order of several kK, the frequency $\nu_{ei} = \nu_{rt}(T_i/T_{rt})$ exceeds the frequency ν_{ee} [64]. Here, ν_{rt} is the collision frequency at room temperature. Then, we have $\kappa = (1/3)v_F^2\gamma T_e/(\nu_{rt}(T_i/T_{rt})) = \kappa_{rt}(T_e/T_i)$. The thermal conductivity κ increases linearly with an increase in the electron temperature, and the coefficient in this linear dependence decreases with an increase in the ion temperature [49, 52, 62, 64].

In the 1T states, the thermal conductivity barely changes: temperatures T_e and T_i in the expression $\kappa = \kappa_{rt}(T_e/T_i)$ cancel each other.

In the situations related to USLPs the density in the heating layer d_T changes only slightly in the 2T stage (isochoricity). The isochoricity is due to the supersonic character of the formation of the heating layer.

The influence of the density variation was considered in [63], where the dependence of κ on the temperature in the binodal was presented and the dependences in the binodal and isochore were compared. The case of semiconductors, which pass to the metallic state at melting, was also analyzed in that study.

Formula $\kappa = \kappa_{rt}(T_e/T_i)$ is valid until the electron–electron scattering starts to exert an influence. In many papers, the frequency ν_{ee} is approximated as $\nu_{ee} \sim T_e^2$. This approximation originates from the well-known classical works in natural science [66, 67]. The proportionality factor in the quadratic approximation is determined from measurements at low temperatures [54] (or from calculations [54]). At low temperatures (the values of which are small in comparison with the Debye temperature), phonon scattering is frozen: frequency ν_{ei} decreases at $T \to 0$ more rapidly than ν_{ee}.

At $T_e \approx 10$ kK, first, the proportionality $\nu_{ee} \sim T_e^2$ becomes invalid. The frequency ν_{ee} increases with an increase in T_e much more slowly: the quadratic dependence is saturated (Fig. 8 in [54]). Second, at $T_e \approx 10$ kK or higher, the frequency ν_{ee} dominates over the frequency ν_{ei} under isochoric conditions that are typical of USLPs [49, 52, 54, 60–64]. The formula $\kappa = \kappa_{\rm rt}(T_e/T_i)$, which describes the linear increase in thermal conductivity with an increase in electron temperature T_e, then becomes invalid. Factor κ increases, but more slowly in comparison with the linear function with argument T_e.

The thermal layer is expanded according to the law $x = 2\sqrt{\chi t}$, where χ is the thermal diffusivity. Up to temperatures on the order of several eV, $\chi = \kappa/C = \kappa/(C_i + C_e) \approx \kappa/C_i$ in the 1T isochoric state, because $C_i \approx 3nk_{\rm B}$ exceeds the electronic specific heat of partially degenerate electrons $C_e = \gamma T_e$ (the atomic concentration is denoted as n). In these states (1T, isochore), the χ value is about 0.1–1 cm^2/s for solid and molten metals.

The situation with thermal diffusivity χ sharply changes upon passing to the 2T states. Indeed, the main difference between the 2T and 1T states consists of the separation of the energy balances for the electron and ion subsystems. This was shown in 1974 in a pioneering work by Anisimov, Kapeliovich, and Perelman [68]. Correspondingly, the specific heat coefficients are also separated. Heat flows via the electron subsystem. The energy is simultaneously slowly transferred to the ion subsystem due to the electron–ion exchange.

The corresponding two heat-balance equations for the case without hydrodynamic motion were given in [68]. The complete system of equations of two-temperature hydrodynamics has been presented, e.g., in [30]. In contrast to the system of equations in [68], the complete system in [30] (in addition to the law of conservation of energy [68]) includes the laws of mass and momentum conservation. The system of hydrodynamic equations [30] is based on the equations of the 2T quasi-thermodynamic state of the medium and descriptions of the kinetic coefficients in the 2T states. Here, we speak of quasi-thermodynamic states, because the relaxation between the electron and ion subsystems in the 2T stage is still incomplete. The thermal equilibrium in the electron subsystem (at fairly large T_e values) is established much more rapidly than the equilibrium with respect to the temperature between electrons and ions (because of the large difference in the masses).

Note also that the range of physical phenomena covered by the 2T hydrodynamics constantly increases. The elastoplastic effects in the target region in the solid state under femtosecond irradiation were taken into account in [69, 70]. Thus, the generalization related to the 2T mechanics of a deformed solid was satisfied.

Another important line of research is related to the influence of electron pressure on the dynamics of the expansion of the target surface layer [7, 71, 72]. The point is that the electron pressure is much higher than the thermal contribution to pressure from the ion subsystem in the early stage of the process (when the main absorbed energy is still concentrated in the electron subsystem). As a result, the material is extended under electron pressure p_e. Notably, above some threshold of electron temperature T_e (~2 eV), some of the surface layer detaches (specifically, a metal layer with electrons in the excited state). The cohesion energy between excited atoms in the detached layer is very low or zero, i.e., the material passes to a gas-like state. Apparently, it is natural to call this phenomenon “cold evaporation” or “cold ablation.” This ablation is referred to as cold, because the ion-subsystem temperature is low in the early stages of the ultrashort irradiation.

The question of the emission of acoustic perturbation by an electron heat wave is important [73, 74]. The perturbation is emitted in the transonic stage of heat-wave propagation. In this stage, the velocity of the initially supersonic heat wave decreases and becomes subsonic. This question is urgent, because the aforementioned perturbation emission affects the ratio between the plastic and elastic waves in a two-front elastoplastic shock wave [73, 74]. The perturbation actually forms an elastic shock wave with a large amplitude. The amplitude of this wave exceeds the conventional amplitudes (which are less than 1 GPa) for elastic waves generated in experiments on explosive materials and strikers.

The expression for the electron thermal diffusivity of metal χ changes under the 2T conditions. Here, we have $\chi = \kappa/C_e$, because the absorbed laser energy is transferred in to the bulk via the electron subsystem. In the 2T states, the coefficient χ increases by a factor of (C_i/C_e). The C_i/C_e ratio is high until the electron temperature is much lower than Fermi temperature $T_{\rm F} \sim$

10^5 K. The C_i/C_e ratio is in the order of magnitude of T_F/T_e.

The above circumstance yields high (supersonic) heat propagation velocities $\dot{x} = \sqrt{\chi/t}$, $x = 2\sqrt{\chi t}$ in the 2T stage. In the first remarkable studies on thermoreflectance [75, 76] performed for thin (~100 nm) films with USLP, the phenomenon of supersonic heating was attributed to the ballistic passage of electrons. The brief term "reflectance" stands for a change in the reflectance of metal upon the heating of its electron subsystem. An important feature of experiments [75, 76] is that the film thickness was smaller than the layer thickness d_T heated in the 2T stage. Indeed, the velocity $\dot{x}$ of the thermal diffusion (not ballistic) expansion of the heating layer is very high in the 2T stage, because it is comparable with the Fermi velocities of electrons ($v_F \approx 1000$ km/s).

Let us write the electron thermal diffusivity of metal χ in the form $\chi = (1/3)\, v_F^2 \tau_e$. We reduce the heat-propagation velocity via the electron subsystem $\dot{x}$ to the speed of sound ($\dot{x}/c_s$) to obtain the effective Mach number for heat propagation. It can be estimated as $\dot{x}/c_s \sim M_F\sqrt{\tau_e/t}$, where $M_F = v_F/c_s \approx 10^2$ is the Mach number for hypersonic electrons. The velocity $\dot{x}$ decreases to the speed of sound for a time on the order of $t_* = M_F^2 \tau_e$. At an electron mean free time τ_e on the order of several femtoseconds (which is valid at $T_e \approx$ 1 eV), we have $t_* \sim 10$ ps. The estimate of the time t_* is comparable with electron–ion relaxation time $t_{eq} \approx 1$ ps. The time t_{eq} is assumed to be either the time $t_{eq}(1)$ of the equalization of temperatures T_e and T_i or the time $t_{eq}(2) < t_{eq}(1)$ in which the majority of the electron energy is transferred to the ion subsystem. Estimates of important 2T scales d_T and t_{eq} with respect to the target-material characteristics and laser-pulse parameters were presented in [30, 77].

In the time range of $0 < t < t_{eq}$ (when the system is in the 2T state), the heat-propagation velocity in the target metal significantly exceeds the speed of sound [78]. This effect was observed in all numerical studies on ablation with USLPs [77–82]. A simple explanation and estimates of the velocity were given above. The supersonic portion is especially noticeable if the (x, t) flow diagram is presented in a paper on a sufficiently small time scale [73, 80, 82]. The (x, t) diagram was shown in Fig. 8 in [73], in which the structure of an elastoplastic shock wave with a complex time evolution was resolved for the first time.

Supersonic heating is the most important circumstance distinguishing USLP regimes in comparison with longer-term irradiations. This circumstance results in the formation of heating layer d_T before the stage of unloading of the heated layer due to rarefaction waves, in which the heated material is thermally expanded. For precisely this reason, the thermomechanical effects manifest themselves at a sufficient absorbed energy F_{abs} (fluence in J/cm^2): the target is ablated because of mechanical detachment of the material (spallation) rather than conventional (in the physics of the interaction between radiation and matter) evaporation. The discovery of this physical–mechanical relationship made it possible to explain [83–86] the occurrence of Newton rings in the experiment [87]; notably, the number of rings was not constant but increased with time [87].

The fact that Newton rings can be seen in the experiments indicates that the spallation shell is partially transparent for diagnostic laser pulses (probe pulses in the pump–probe schematic). Since the rings can also be observed in metals [87], the shell thickness is on the order of skin-layer thickness $\delta_T = 10$–20 nm or much smaller, i.e., the occurrence of the phenomenon of nanospallation, which had been unknown prior to [83, 87].

Newton rings were found with the pump–probe technique (which is based on the stroboscopic principle) [87–93]. Pump–probe interferometry was applied later [88–90, 92]. Japanese researchers generalized the pump–probe approach for both Newton rings and interferometry (with a double Lloyd mirror) to the case in which the probe pulse is a laser beam with 90-eV photons at a wavelength of 13.9 nm (vacuum ultraviolet–soft X-ray spectral region) [94].

Detailed information about processes occurring for extremely short time intervals has been obtained with Newton rings and interferometry [95, 96]. The efficiency of these techniques was shown [95, 96]. They yield kinematic information (instantaneous positions and velocities of reflecting boundaries) and data on the physical state (via analysis of optical data on the permittivity). In this context, concerning the kinetic data, the above techniques may replace the popular VISAR, ORVIS, and PDV systems (the time resolution is as high as several tens of ns) [97–103] in experiments for which a time resolution on the order of 0.1 ps is required [87–96].

At not very high temperatures, unloading after USLPs occurs at hydrodynamic velocities that are much lower than the speed of sound [104]. The stage of active motion begins at times on the order of $t_s = d_T/c_s$. The high pressure in the heating layer drops, and a pair of compression and rarefaction waves is generated [89] to escape into the bulk. Other important phenomena (e.g., cavitation, foaming, and spallation) [3, 4, 7, 9, 13, 14, 17, 80, 82, 105–110] are related to evolution of the entropy-vortex layer (hot disk in Fig. 1). These phenomena occur under a mechanical momentum that is transferred to this layer upon the reflection of the compression wave from the interface between the target and the matter (or vacuum) [3, 4, 7, 9, 13, 14, 17, 80, 82, 105–110] with an acoustic impedance that is small in comparison with the acoustic impedance of the target material. The phenomena of cavitation, foaming, and shell spallation caused by USLPs are universal in the sense that they are observed under both optical and X-ray laser irradiations [9, 17, 94, 109, 110].

2. CLASSIFICATION OF REGIMES: PULSE-WIDTH VALUE

As stated above, the description of the arising motion is based on the duration τ_L of the laser irradiation of the target and the thickness of the heated layer d_T. The thickness d_T and the speed of sound compose an acoustic time scale of $t_s = d_T/c_s$. The ratio of the time t_T of layer formation d_T and the scale t_s plays a decisive role. This ratio underlies the classification of laser regimes at a moderate pulse power, when, on the one hand, the effect causes significant hydrodynamic consequences (melting and ablation) and, on the other hand, the maximum temperatures are limited to the order of several tens of eV. Note that this range is important for most technological applications of lasers: product treatment, welding, cutting, drilling, the formation of surface structures, hardening, nanoparticle production, etc.

If $t_T \ll t_s$, the heating is supersonic and the pulse is referred to as ultrashort. During time t_T, the pressure in layer d_T increases. Then, at a time of $\sim t_s$, the high-pressure layer is decomposed according to d'Alembert [89]. This means that the two acoustic compression waves carry away the high pressure from the plane layer d_T upon their exit. Since one of the waves propagates toward the target boundary, this wave is reflected from the latter. If the acoustic impedance of the medium is small beyond the target boundary, the reflected compression wave is transformed into the tensile one. In this wave, entropy-vortex layer d_T is extended toward the environment. The surface layer d_T remains a high-entropy layer after the passage of the acoustic compression wave and tensile wave. A vortex flow is formed at the lateral boundary of the hot spot in Fig. 1.

The physical parameters are such that femtosecond–picosecond pulses ($\tau_L \approx$ 10 fs–1 ps) can be considered USLPs. The heating thickness d_T is 30–40 nm for metals with low thermal conductivity and a large α parameter. This parameter determines energy transfer rate $\dot{E} = \alpha(T_e - T_i)$ W/m^3 from the electron subsystem to the ion subsystem. The above group of metals include nickel [49, 50], platinum [49, 50], palladium, ruthenium [52], etc., with $\alpha \approx 10^{18}$ W m^3/K. The speed of sound in these metals is 4–5 km/s. Correspondingly, the acoustic scale is t_s = 6–10 ps. The electron–ion relaxation time t_{eq} in these metals is about 1 ps. Pulses with a width of $\tau_L < t_s$ can be considered USLPs. If $\tau_L < t_{\text{eq}}$, the pronounced 2T stage is observed. In the case of $t_{\text{eq}} < \tau_L < t_s$, the 2T stage is weakly pronounced; however, the effect still belongs to the USLP class.

In gold, the thickness d_T reaches a maximum value of about 150 nm. The speed of sound in gold is low (3.1 km/s). Therefore, the acoustic scale t_s is large (up to 50 ps). The electron–ion relaxation in gold is slow (t_{eq} = 5–10 ps) in comparison with other metals. For durations of 10 ps < τ_L < 50 ps, the 2T stage in gold is weakly pronounced.

At $\tau_L \approx t_s$, there is a boundary between USLPs (supersonic heating) and long pulses with subsonic heating. The ablation flow changes qualitatively at the region edges: $\tau_L \ll t_s$ and $\tau_L \gg t_s$. The former case ($\tau_L \ll t_s$) is characterized by the ablation threshold. Above the threshold (at $\tau_L \ll t_s$), thermomechanical detachment of the target material layer occurs. The threshold is determined by the tensile strength of the condensed phase (generally, melt) and is pronounced [111–116]. Ablation was studied in those works with USLPs for gold, tin, iron, tantalum, and molybdenum.

Note, incidentally, that USLPs are also used to measure the spallation threshold in a solid phase when a shock wave exits the rear film side [111, 112, 117, 118]. Submicron and micron films are generally used in such experiments. The structure of the shock wave front is determined in the same experiments. The elasticity threshold was found to sharply increase in ultrashort shock waves. The difference between the front ablation and rear spallation and the details of the propagation of a laser-induced shock wave in the case of USLPs were clarified in [112].

Spallation from the side of the irradiated boundary is referred to as ablation. The break generally occurs in the melt layer. The strength threshold depends on the liquid-phase temperature in the layer in which the break occurs [111–116].

In the second case ($\tau_L \gg t_s$), the mechanical detachment is replaced with purely thermal evaporation. The 2T stage is absent. The target temperature is approximately proportional to absorbed energy F_{abs}. The saturated vapor pressure is given by a finite exponential function, which turns to zero only at zero temperature. Therefore, evaporative ablation, generally speaking, has no threshold, although the amount of material evaporated in vacuum rapidly (exponentially) increases with an increase in F_{abs}. Comparison of these two cases relative to the expenditure of energy to remove a gram of the target material shows that the ablation regime with USLPs is more energy-efficient (by a factor of 3–5) than pure evaporation [106]: the ratio of a gram of removed material to the spent energy is three to five times lower.

In the case of $\tau_L \gg t_s$, the pressure is always positive. One can see no reflection of the compression wave from the boundary and no mechanical foaming of the entropy-vortex layer due to tensile stress and spatial extension [32–34]. Note that the acting pulse can be considered a USLP not only when its duration falls in the femtosecond–picosecond range. The acoustic scale t_s is determined by the heating depth d_T. For example, the effect of a relativistic electron beam on aluminum with an electron mean free path of 1 μm yields an acoustic scale t_s of 200 ps.

Note that the melting regimes in the opposite cases under consideration ($\tau_L \ll t_s$ and $\tau_L \gg t_s$) radically differ. At $\tau_L \ll t_s$, melting in the stage $t < t_{\text{eq}}$ of supersonic heat transport by electrons occurs in the homogeneous regime [78]. This means that there is no sharp melt front: a fraction of the liquid phase in the mixture of the liquid and solid phases gradually increases in a wide layer with a thickness on the order of d_T. The increase in this fraction is due to the heating of the ion subsystem via internal heat transfer from the hot-electron subsystem with the coupling term $\dot{E} = \alpha(T_e - T_i)$. This melting occurs in the isochoric regime (i.e., under high pressure). The pressure increases the melting temperature $T_m(p)$. Therefore, when the compression wave leaves the entropy-vortex layer d_T, the pressure decreases, as does the melting temperature. Accordingly, an additional portion of material is melted quite rapidly [73].

With subsonic laser irradiation ($\tau_L \gg t_s$), conversely, the melting occurs in the classical heterogeneous regime. There is a sharp melt front with a thickness on the order of several interatomic distances. Heat flux arrives at the front from the hot surface layer of the target. Some of this flux passes behind the front and is spent on heating the solid phase before the front. The other part is spent on melting the solid phase, due to which the front moves toward the solid phase. There are small jumps in pressure and hydrodynamic velocity at the melt front [119] (the amplitude of the velocity jump is small in comparison with the speed of sound). The occurrence of discontinuities in pressure and velocity is caused by the expansion of the material upon melting.

There is a transition region $\tau_L \sim t_s$ between the extreme regimes $\tau_L \ll t_s$ and $\tau_{\text{L}} \gg t_s$ (subsonic heating). Here, the thermomechanical ablation is gradually transformed into an evaporative regime with an increase in the τ_L/t_s ratio to a value of on the order of unity. At an identical absorbed energy F_{abs}, the pressure in the heating layer decreases with an increase in the τ_L/t_s ratio. At small τ_L/t_s values, the pressure is determined by F_{abs} and does not depend on the τ_L/t_s ratio. The thermomechanical-ablation threshold $F_{\text{abs}}|_{\text{abl}}(\tau_L/t_s)$ somewhat increases when the τ_L/t_s ratio becomes higher than a value on the order of unity. Beginning at a certain (critical) τ_L/t_s value, thermomechanical ablation does not occur. These questions were discussed in [32], in which the calculation results for different durations τ_L were compared.

3. CLASSIFICATION OF REGIMES: CONFINEMENT VALUE

Let us consider how the presence or absence of fairly dense condensed matter contacting with the target affects ablation. Figure 1 shows different versions of laser-beam delivery to the surface of the absorbing target. These versions imply transmission through vacuum, air, or transparent condensed matter. The condensed phase includes two subversions, with solid and liquid transparent condensed matters. For definiteness, we will compare condensed matters with vacuum. For the considered luminous fluxes, the case with air is approximately equivalent to the case with vacuum; chemical phenomena (like target oxidation in air) call for a separate analysis.

The inertia of the medium that receives the laser plume (laser ejection) is important. There is a clear difference between, on the one hand, the case of vacuum/air with a ratio of the target density to the receiving (external) medium density of $\mu = \rho_{\text{target}}/\rho_{\text{extern}}$, which ranges from infinity to a value on the order of 10^3, and, on the other, the case of a condensed environment with density ratios of 1 : 1 (aluminum : glass) or 20 : 1 (gold : water). A medium with a low density usually has a smaller acoustic impedance. The impedance ratio determines the flow character. Obviously, a change in the ratio μ by three orders of magnitude qualitatively affects the behavior of the material ejected from the target. The question of the effect of the ratio μ was considered in works by Povarnitsyn [29] and Zhigilei et al. [120]; cases with $\mu = \infty$ and $\mu \sim 1$ were compared. It was shown that a free spread of ablation products occurs at $\mu = \infty$, whereas the environment makes a very strong retarding effect on the spread of target ablation products at $\mu \sim 1$–10. This circumstance was noted in all numerical studies on LAL [27–34, 119]. This effect is used in LAL for the retention of ablation products and their fragmentation/condensation into nanoparticles.

There is a significant difference between solid and liquid receiving media. The heating of an absorbing metal through a transparent glass was analyzed in [55, 73, 121–125]. These studies are related to the USLP effect. Longer pulses were studied numerically in [126]. These calculations were performed in relation to experiments by Delaporte's group [127–130].

Veiko proposed an original technique for the laser drilling of spinnerets in diamonds. A long (10–100 ns) laser pulse is used, and the diamond surface is adjacent to solid graphite. This technique can efficiently replace mechanical drilling methods. Diamond spinnerets (drawing dies) are widely used for drawing wires. The approach with diamond drilling was developed in [131] (see also the study [132] on laser etching of sapphire). We note here the reviews [133, 134] on the breakdown and structuring of insulators and polymers.

The classification of regimes can briefly be presented as follows. First, nucleation, foaming, and the formation of a spallation shell are characteristic of quite short pulses with a duration τ_L on the order of t_s or smaller. This conclusion is valid irrespective of the μ value for the target and transparent medium. Second, the behavior of the plume of ablation products is determined by the μ ratio. In addition, in the case of $\tau_L > t_s$, the recoil momentum transferred to the target significantly increases in the presence of a liquid (see, e.g., [45, 46, 119, 135]).

4. ABLATION IN LIQUID: INFLUENCE OF THE IRRADIATION DURATION

The hot disk in Fig. 1 consists of several layers. The phase compositions of the target material and the material around the target (in the case of confinement of the target by a condensed phase) in these layers change because of the heating gradient (in the direction perpendicular to the surface). The target contains a shock-compressed layer, a melt layer, a metal layer in the two-phase (liquid—vapor) state, and, with a sufficiently large contribution of the laser energy to the disk, a gas-plasma layer composed of the target material. In the external condensed matter, the heated disk of environment material is adjacent (from outside) to the metal disk. It was stated above that the disk is thin because $R_L \gg d_T$ as a rule.

The hydrodynamics of compressible media divides perturbations into acoustic modes and the entropy-vortex mode. For example, if a compact region is heated in a homogeneous medium, acoustic perturbations are emitted from this region. Acoustic modes diverge with the speed of sound from the heating region. The entropy-vortex mode is frozen into the material and moves with the hydrodynamic velocity of this substance. This division into modes is applicable for the case shown in Fig. 1. Acoustic perturbations leave the hot disk, and the disk material is stiff relative to sound perturbations. In problems with laser irradiation, the disk material remains hot for a long time. The cooling process lasts for many acoustic time scales $t_s = d_T/c_s$.

There is an important specificity in the cases with division into acoustic and entropy-vortex modes. The point is that the heating region is located at the target boundary rather than in the bulk of the homogeneous material (notably, the medium with a lower acoustic impedance is on the outside). The reflection of an acoustic pulse from the boundary in the case of USLPs is accompanied by extension of the heating layer d_T (the localization domain of the entropy-vortex mode). The extension of layer d_T at a fairly large extension amplitude induces nucleation, foaming, and the formation of the spallation shell.

Figure 2 shows the intermediate stage (stage II) of the evolution shell. In the initial stage (stage I), the heating region was a thin disk (see Fig. 1). Shock waves rapidly (in comparison with the material expansion velocity in the hot disk) propagate from this disk into the liquid and target bulk. The structure shown in Fig. 2 gradually forms in times on the order of 10—100 ps. The temperature of the shock-compressed liquid (for definiteness, water) is low and differs only slightly from the initial temperature. Hot water forms a layer *2* around spallation shell *3*.

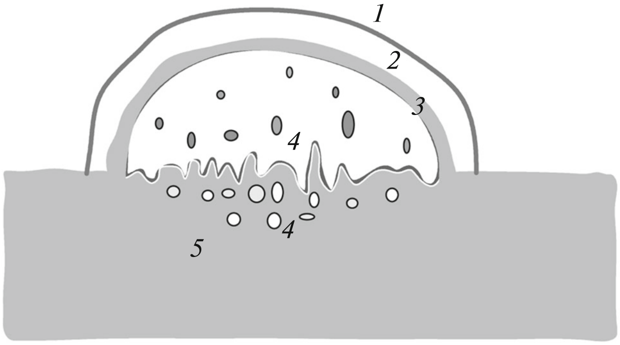

Fig. 2. Structure of the flow with ablation in liquid after the USLP effect at stage II: (*1*) shock-compressed liquid, (*2*) hot liquid, (*3*) spallation shell, (*4*) foam, and (*5*) liquid phase of the target material.

Foam *4* is beneath shell *3*. The liquid phase of the target material *5* is under the foam at stage II. The solid matter of the target that passed through the shock wave is underneath the melt *5*. The shock wave in the target is deep below the region shown in Fig. 2. The foam consists of liquid phase and vapor. The difference in pressure above and below the shell slows the spallation shell. Under the shell, the pressure is equal to the saturated vapor pressure. The melt density in shell *3* (Fig. 2) is higher than the hot-water density in layer *2*. The well-known [136, 137] Rayleigh—Taylor instability develops due to the difference between the densities at the interface between media *2* and *3* and the retardation of this interface.

The instability at the interface between media *2* and *3* was studied in [27, 30, 138]. The instability begins with the capillary scale $\lambda_{\rm cap}$, which is several tens of nanometers with the parameters chosen in [27, 30]. The shell thickness increases because of the accretion of foam fragments [30] on the shell inner surface (interface *3*—*4* in Fig. 2). The fact is that the shell velocity decreases due to retardation by the liquid, and the detached fragments move with a constant velocity. A similar situation (deposition of foam on the shell) is observed in shells that are retarded due to the surface tension rather than the environment [139]. In [27, 30], the wavelength $\lambda_{\rm cap}$ was smaller than the shell thickness $h_{\rm sh}$. This means that the development of the Rayleigh—Taylor instability is not yet significant for the shell integrity.

In the long run, retardation of the shell leads to its stoppage and backward motion. The time of the stop

t_{stop} is several tens of nanoseconds, and the distance traveled h_{stop} is several to several tens of μm. Lasers with a high pulse energy (several joule or higher) are generally applied in nanoparticle production technologies. The radius of the irradiation spot R_L (Fig. 1) can then be increased to about 1 mm. In this case, the shell form during fracture is quasi-planar: $h_{\text{stop}} \ll R_L$. In the case of small spots ($R_L \sim h_{\text{stop}}$), a significantly curved shell (such as that in Fig. 2) undergoes decay at equal horizontal and vertical scales of the length (examples of these calculations were given in [105, 140]). The transverse sizes of the evolving shell can never exceed the laser-spot radius. At $h_{\text{stop}} \ll R_L$, the horizontal shell sizes in Fig. 2 are much larger than the vertical length.

Will the shell that turns back reach the target surface, or will it decompose into capillary fragments before it gets there?

First, we should note the following. The shell *3* forms in the case of USLPs (Fig. 2), which is at a finite distance from the crater bottom, in a time of about 10 ns. During this time, the melt *5* (Fig. 2) covering the crater bottom is cooled and crystallized; the freezing process was analyzed in detail in earlier studies. Freezing of the foam residues leads to the formation of a solidified, random micro- or nanorelief as described in [1–16]. Thus, this surface structure forms regardless of whether the ablation products are ejected into vacuum or liquid.

Kudryashov's group carried out remarkable experiments [14, 141] that strictly confirm this simple conclusion. These works showed that identical, random surface reliefs remain after the USLP effect through air and liquid.

Now we revert to the question stated above: will the shell moving backwards reach the bottom crater? Apparently, the shell decomposes before it collides with the crater bottom. Indeed, no significant traces of the backward shell were observed on the crater bottom in [14, 141]. Note, incidentally, that the formation of a random surface nanostructure and the shell decomposition occur on time scales that are small in comparison with the bubble-formation time (several microseconds). Apparently, the shell destruction *3* (Fig. 2) is responsible for the formation of a fraction of large nanoparticles. Small nanoparticles form due to the condensation of metal vapor that evaporated into the liquid.

5. ABLATION IN LIQUID UPON NANOSECOND IRRADIATION

Ablation caused by a nanosecond laser pulse differs significantly from the case of USLPs considered in the previous section. With nanosecond ablation, there is no nucleation in the target material on the irradiated side; accordingly, there is neither foam nor spallation plate. The point is that the pressure remains positive all the time (mechanical extension by inertia is absent).

Here, we consider an example with no thermomechanical ablation in the case of LAL. Laser radiation passed through a transparent liquid is absorbed to form the hot thin disk shown in Fig. 1. The acoustic time scale t_s is small in comparison with the pulse duration $\tau_L = 0.5$ ns set by the Gaussian function $I(t) \sim \exp(-t^2/\tau_L^2)$ in the calculation. The energy absorbed in the target is 0.9 J/cm^2 in this calculation. The numerical simulation begins at instant $-3\tau_L$.

Since the t_s/τ_L ratio is small, the disk thickness in Fig. 1 increases by several times during the laser pulse. This increase is caused by constantly supply of energy from the laser to the disk. The moving upper and lower disk boundaries in Fig. 1 act like pistons, which maintain shock waves in the liquid and metal, respectively [119, 135]. This situation qualitatively differs from the d'Alembert decomposition of the high-pressure layer in the case of USLPs. It follows from the estimations [135] that the pressure in the disk under nanosecond irradiation changes according to the law $p \propto \sqrt{I(t)}$. The calculations show that this law is approximately satisfied. However, there are some specific features that should be discussed.

Let us describe the evolution of the flow caused by a pulse with $\tau_L = 0.5$ ns and $F_{\text{abs}} = 0.9$ J/cm^2. Figure 3 shows the situation not long before the maximum of the nanosecond pulse. We assume that the laser beam passes through the water layers and is absorbed in the skin layer of gold near contact II with water. Therefore, the maximum temperature is in contact II. The absorbed energy is mainly transferred to the gold bulk via heat conduction of gold. The heat transfer to the water is small, because its thermal conductivity is lower than the gold thermal conductivity. The heating of the metal leads to the formation of a liquid-phase layer. The melt front is at point I. The temperature kink is at point I. The reason is that, first, some of the heat flux is spent on melting (front I moves in the material to the right) and, second, the thermal conductivity in solid gold is higher than that in the liquid phase.

The pressure profile at the same instant as in Fig. 3 is presented in Fig. 4 along with the density. Note that there is quite an unexpected specific feature of the pressure distribution. The pressure is maximum not in the skin-layer region, where the laser energy is absorbed. The skin-layer regoin contains the temperature maximum shown in Fig. 3. It was found that, in the intense-heating stage (which approximately corresponds to the middle of the heating pulse), the pressure maximum is slightly behind the melt front I in Figs. 3 and 4. In addition, there is a pressure jump related to the material expansion at melting. The melting is likely to cause the aforementioned displacement of the pressure maximum. A pressure drop at the melt front is required to ensure that the melt outflow has a larger specific volume in comparison with the solid

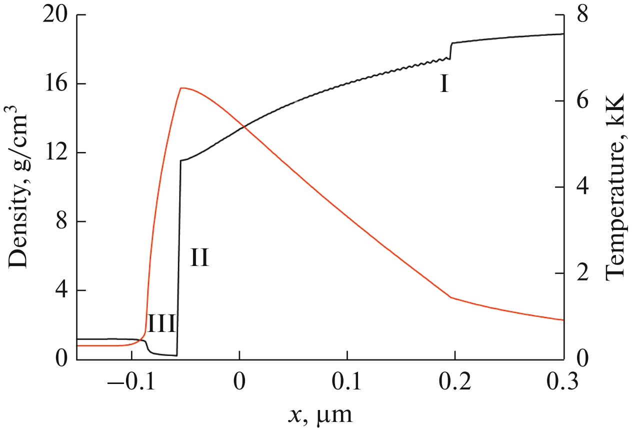

Fig. 3. Instantaneous density and temperature profiles at instant of –0.2 ns: (I) heterogeneous melt front, (II) contact between hot gold and hot water, (III) hot-water layer heated due to the heat conduction of water via contact with hot gold.

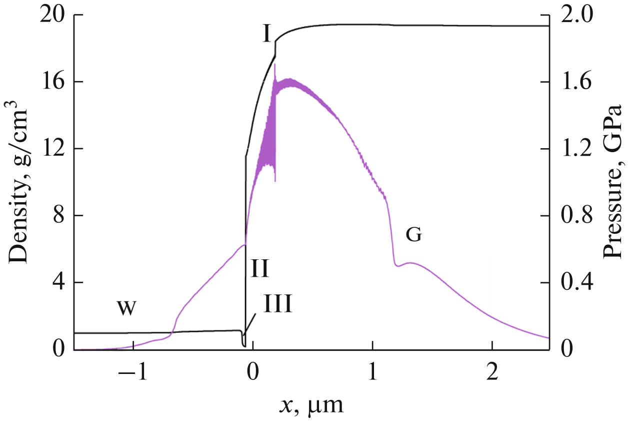

Fig. 4. Instantaneous density and pressure profiles at –0.2 ns. Roman numerals I, II, and III are taken from Fig. 3; their meanings are the same. Letters W and G indicate the nucleation regions of future shock waves in water and gold, respectively.

phase. A further decrease in density then begins on the contact II side due to the heating of the gold by the heat flux from the contact. This expansion process calls for a pressure gradient that mechanically supports the expansion.

Figure 5 shows a comparison of the pressure profiles at instants of –0.2 ns and 0 (which corespond to the intensity maximum). At these instants, 29 and 50%, respectively, of the total absorbed energy F_{abs} = 0.9 J/cm^2 were absorbed in the gold. The heat flux in the time interval from –0.2 ns to 0 is 21% of F_{abs} = 0.9 J/cm^2. This energy additive increases the pressure amplitude at the pressure maximum and in gold near contact II (Fig. 5). Note also that the breaking of the compression wave upon the occurrence of the shock wave due to the focusing of characteristics occurs at times on the order of the pulse width.

At t = 0, the intensity passes through the maximum. However, the absorbed energy continues to increase afterward. Figure 6 shows the corresponding evolution of the pressure profiles in the decaying part of the laser pulse. The pressure maximum continues to increase after passing through the intensity maximum. Thus, the instant of maximum pressure is shifted in time with respect to the intensity maximum. Note that the pressure maximum shifts to the right, i.e., it leaves the region immediately behind the melt front. The melting rate gradually decreases because of the decrease in intensity.

The onset of the formation of the pressure drop can clearly be seen in Fig. 6. The pressures formed by the piston motion (the motion of the expanding region of radiation absorption and heating) in earlier stages of the laser-pulse effect shift to the right and to the left along the characteristics. In the earlier stages, the intensity $I(t)$ is higher, and the expansion occurs at higher velocities; therefore, the pressures moving away from the heating region by the characteristics are higher.

Figure 7 gives the further evolution of the flow. A deep hole in pressure arises around the destroyed absorption region (the radiation intensity at instant t = 2 ns is $e^{-16} = 10^{-7}$ of the intensity at the pulse maximum). Expansion of the hole occurs in the course of time, because the characteristics that cause small pressure values are now emitted from the former absorption region. Note that the high-temperature region continues to exist in the sense of the emission of characteristics causing small (but not zero) pressure values.

Comparison of the two profiles in Fig. 7 shows that a full-fledged triangular shock wave forms in water. The triangularity of its form indicates that this wave is gradually damped during propagation. The point is that the flow behind the front is subsonic; therefore,

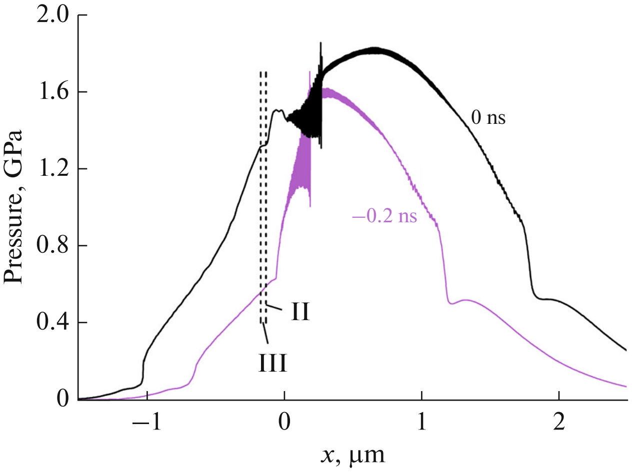

Fig. 5. Pressure profiles at –0.2 ns and 0: (II) the position of the contact and (III) hot-water layer at t = 0.

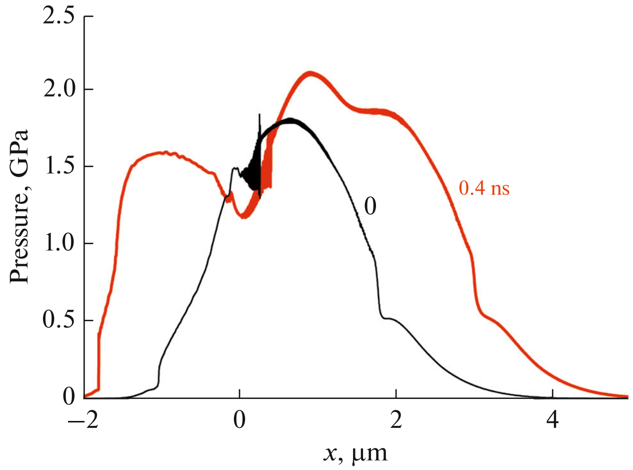

Fig. 6. Pressure profiles at 0 and 0.4 ns; the profile for $t = 0$ is taken from Fig. 5.

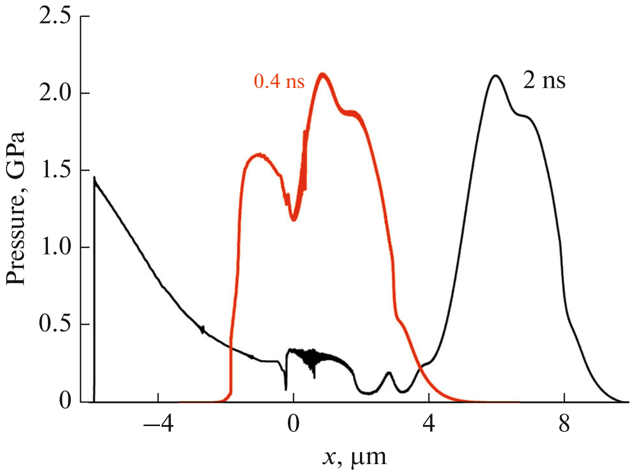

Fig. 7. Evolution of the pressure distributions after the end of the pulse.

the characteristics with low pressures arrive at the front and weaken it. The damping of the compression wave in gold is small. The compression wave amplitude (about 2 GPa) is only 1% of the gold bulk modulus $B = 180$ GPa. Thus, the wave in gold is, in fact, a linear acoustic wave. The situation with water is different. The bulk modulus of 2.2 GPa is comparable with the wave amplitude in water. Correspondingly, the wave in water is strongly nonlinear (shock). This wave is significantly damped during propagation. With a decrease in the wave amplitude in water, it is also transformed into a weakly linear wave. However, the triangular wave shape formed in previous stages is retained.

It is noteworthy that, despite the termination of heating of the contact region by the laser pulse, the pressure in the heating layer does not drop to zero (Fig. 7). The formula $p \propto \sqrt{I(t)}$ does not describe the tail of the pressure pulse, which continues to affect gold and water after the complete termination of laser heating. This "aftershock" effect is especially significant in the case of moderately long pulses (about 1 ns).

Figure 8 illustrates a further stage of flow evolution. The wave amplitude in water decreases from about 15×10^3 to 3×10^3 atm. As can be seen, the pressure near the contact remains significant: about 2000 atm at $t = 2$ ns and 300 atm at $t = 36$ ns. The question arises as to the physical cause responsible for the maintenance of this pressure.

Figure 9 shows the velocity profile. The velocity behind the shock-wave front in water remains significant (about 10% of the speed of sound in water at room temperature). The motion in gold stops beginning at quite early stages, and the velocity of gold is about zero; gold is almost immobile (it moves very slowly to the right and continues to be slightly compressed, Fig. 10). The compression wave in gold at a time of 36 ns (Fig. 9) is far to the right of the contact (at a distance of more than 100 μm from the contact). The maintenance of the pressure in water and gold is related to the continuing expansion of thin (relative to the scales of several tens of μm) hot-water and gold layers. The location of these layers is indicated by an arrow in Fig. 9. Specifically, this expansion pushes water at a time of 36 ns from immobile gold with a velocity of about 25 m/s.

Figure 10 shows the expansion region in more detail. It can be seen how the expansion velocity increases. The hot-water and gold layers (each ~1 μm thick) are separated by contact II. Diffusion was disregarded in the author's Lagrangian code.

The red arrow in the figure highlights the instantaneous velocity distribution along the coordinate and

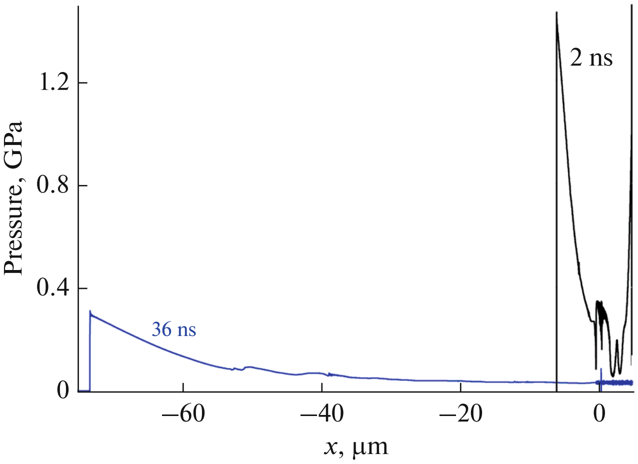

Fig. 8. Penetration of a triangular, weakly non-linear wave (the pressure is 14% of the water bulk modulus) deep into the water (the profile at $t = 36$ ns); the profile at $t = 2$ ns is taken from Fig. 7; the portion related to deep gold layers is omitted.

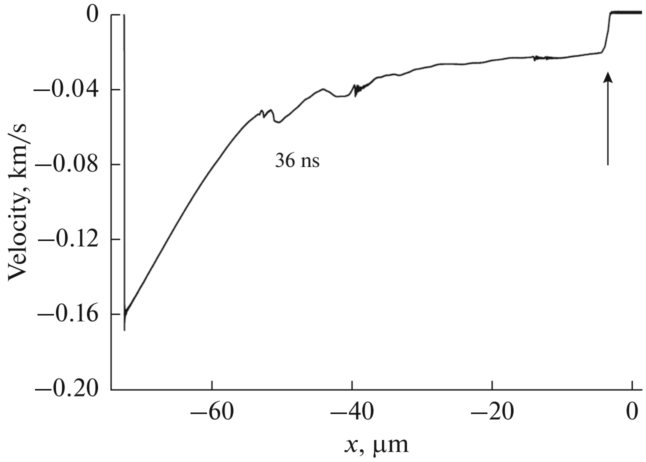

Fig. 9. Velocity profile at 36 ns.

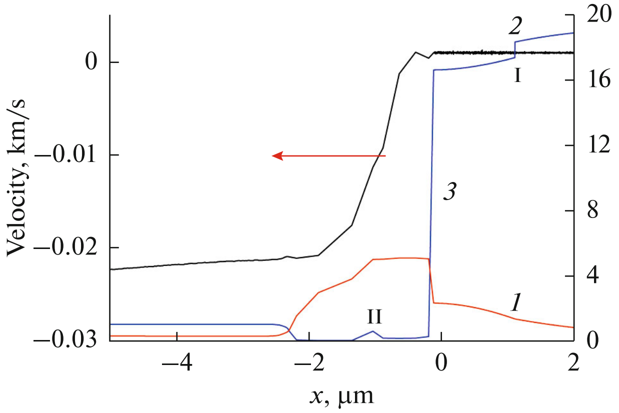

Fig. 10. Hot layer of hot gold vapor and hot water at supercritical pressure of 300 atm: (*1*) temperature profile, (*2*) density profile, and (*3*) vapor–liquid interface.

points to the vertical velocity axis on the left. The vertical axis on the right shows the density values in g/cm^3 for curve *2* and temperature values in kK for red curve *1*.

The velocity behind the shock-wave front decreases to 160 m/s. Gold located to the right of the arrow is almost immobile. The increase in the velocity from the contact with gold is important for pressure maintenance. This increase occurs in the hot-water and gold layers due to their continuing volume expansion.

The interface between the liquid and solid phases of gold is indicated by roman numeral I in Fig. 10. Interface *3* separates the dense liquid gold phase on the right and evaporated gold on the left. Roman numeral II indicates the gold–water interface. Now this is an interface between gold vapor and hot water. The water and gold layers composing the hot layer are ~1 μm thick each. The temperature in the layer at the shown instant is from 3 to 4 kK. If it were not for this hot layer and its expansion, the pressure in water would drop below 300 atm (the pressure at time of 36 ns in the contact region, Fig. 8).

CONCLUSIONS

Laser technologies have made a significant contribution to the formation of the modern world. For example, popular devices like the mobile phone contain no parts prepared without the application of a laser. The physical aspects of important applied problems were analyzed in this study. Problems related to nanoparticle production with laser ablation in liquid were described, surface nanostructuring was considered in detail, and the state of the field of science related to laser forging/peening (the hardening of materials in a laser shock wave) was presented.

It was shown that ablation regimes depend on the presence or absence of confinement of the expansion of a heated target. The case in hand is the heating of a target by a laser beam passing through condensed matter (confinement is present) or through vacuum (confinement is absent). The case with confinement is also divided into versions with solid and liquid confining media.

The division of regimes with respect to the rate of energy injection into the target plays an important role. If a heating layer with a thickness of d_T is formed for a time shorter than the acoustic time scale $t_s = d_T/c_s$, there is a rapid formation of a high-pressure layer with a thickness of $\sim d_T$ and its decomposition with the emission of acoustic waves according to d'Alembert. In the opposite case, the ablation flow evolves in a different way. This evolution was studied in detail in this paper. It was shown that the pressure maximum is shifted to longer times relative to the intensity maximum. It was found that a fairly high pressure in the contact region between the target and liquid is maintained after the cessation of the laser pulse. It turned out that the long-term expansion of hot near-contact layers of target vapor and hot high-entropy water ensures a slow decrease in pressure near the contact. At long times (which are beyond the scope of this study), the diffusion-mixed, high-entropy layers of the target vapor and water form a bubble in the cold, surrounding liquid during expansion ([33, 34]).

REFERENCES

1. Vorobyev, A.Y. and Guo Chunlei, *Opt. Express*, 2006, vol. 14, no. 6, p. 2164.
2. Vorobyev, A.Y. and Guo Chunlei, *Appl. Phys. Lett.*, 2008, vol. 92, 041914.
3. Ashitkov, S.I., Komarov, P.S., Ovchinnikov, A.V., Struleva, E.V., Zhakhovskii, V.V., Inogamov, N.A., and Agranat, M.B., *Quantum Electron.*, 2014, vol. 44, no. 6, p. 535.
4. Ashitkov, S.I., Romashevskii, S.A., Komarov, P.S., Burmistrov, A.A., Zhakhovskii, V.V., Inogamov, N.A.,

and Agranat, M.B., *Quantum Electron.*, 2015, vol. 45, no. 6, p. 547.

5. Vinogradov, A.P., Dorofeenko, A.V., Merzlikin, A.M., and Lisyansky, A.A., *Phys.—Usp.*, 2010, vol. 53, no. 3, p. 243.
6. Nivas, J.J.J., Allahyari, E., Cardano, F., Rubano, A., Fittipaldi, R., Vecchione, A., Paparo, D., Marrucci, L., Bruzzese, R., and Amoruso, S., *Sci. Rep.*, 2018, vol. 8, no. 1, 13613.
7. Inogamov, N.A., Zhakhovsky, V.V., Khokhlov, V.A., Ashitkov, S.I., Emirov, Yu.N., Khichshenko, K.V., Faenov, A.Ya., Pikuz, T.A., Ishino, M., Kando, M., Hasegawa, N., Nishikino, M., Komarov, P.S., Demaske, B.J., Agranat, M.B., Anisimov, S.I., Kawachi, T., and Oleynik, I.I., *J. Phys.: Conf. Ser.*, 2014, vol. 510, 012041.
8. Florian, C., Deziel, J.-L., Kirner, S.V., Siegel, J., and Bonse, J., *Nanomaterials*, 2020, vol. 10, p. 147.
9. Inogamov, N.A., Zhakhovsky, V.V., Ashitkov, S.I., Emirov, Yu.N., Faenov, A.Ya., Pikuz, T.A., Ishino, M., Kando, M., Hasegawa, N., Nishikino, M., Kawachi, T., Agranat, M.B., Andriash, A.V., Kuratov, S.E., and Oleynik, I.I., *J. Phys.: Conf. Ser.*, 2014, vol. 500, 112070.
10. Abou-Saleh, A., Karim, E.T., Maurice, C., Reynaud, S., Pigeon, F., Garrelie, F., Zhigilei, L.V., and Colombier, J.P., *Appl. Phys. A*, 2018, vol. 124, p. 308.
11. Valev, V.K., Denkova, D., Zheng, Xuezhi., Kuznetsov, A.I., Reinhardt, C., Chichkov, B.N., Tsutsumanova, G., Osley, E.J., Petkov, V., Ben de Clercq, Silhanek, A.V., Jeyaram, Y., Volskiy, V., Warburton, P.A., Vandenbosch, G.A.E., Russev, S., Aktsipetrov, O.A., Ameloot, M., Moshchalkov, V.V., and Verbiest, T., *Adv. Mater.*, 2012, vol. 24, OP29.
12. Kudryashov, S.I., Levchenko, A.O., Danilov, P.A., Smirnov, N.A., Rudenko, A.A., Melnik, N.N., Busleev, N.I., and Ionin, A.A., *Appl. Phys. Lett.*, 2019, vol. 115, 073102.
13. Rudenko, A., Colombier, J., Hohm, S., et al., *Sci. Rep.*, 2017, vol. 7, p. 12306.
14. Kudryashov, S.I., Saraeva, I.N., Lednev, V.N., Pershin, S.M., Rudenko, A.A., and Ionin, A.A., *Appl. Phys. Lett.*, 2018, vol. 112, 203101.
15. Remnev, M.A. and Klimov, V.V., *Phys.—Usp.*, 2018, vol. 61, no. 2, p.157.
16. Ionin, A.A., Kudryashov, S.I., Levchenko, A.O., Makarov, S.V., Saraeva, I.N., Rudenko, A.A., Butsen, A.V., and Burakov, V.S., *JETP Lett.*, 2017, vol. 106, no. 4, p. 268.
17. Inogamov, N.A., Zhakhovsky, V.V., Ashitkov, S.I., Emirov, Yu.N., Faenov, A.Ya., Petrov, Yu.V., Khokhlov, V.A., Ishino, M., Demaske, B.J., Tanaka, M., Hasegawa, N., Nishikino, M., Tamotsu, S., Pikuz, T.A., Skobelev, I.Y., Ohba, T., Kaihori, T., Ochi, Y., Imazono, T., Fukuda, Y., Kando, M., Kato, Y., Kawachi, T., Anisimov, S.I., Agranat, M.B., Oleynik, I.I., and Fortov, V.E., *Eng. Failure Anal.*, 2015, vol. 47, p. 328.
18. Kuchmizhak, A., Vitrik, O., Kulchin, Yu., Storozhenko, D., Mayor, A., Mirochnik, A., Makarov, S., Milichko, V., Kudryashov, S., Zhakhovsky, V., and Inogamov, N., *Nanoscale*, 2016, vol. 8, p. 12352.
19. Pavlov, D., Syubaev, S., Kuchmizhak, A., Gurbatov, S., Vitrik, O., Modin, E., Kudryashov, S., Wang, X., Juodkazis, S., and Lapine, M., *Appl. Surf. Sci.*, 2019, vol. 469, p. 514.
20. Ionin, A.A., Kudryashov, S.I., and Samokhin, A.A., *Phys.—Usp.*, 2017, vol. 60, no. 2, p. 149.
21. Makarov, G.N., *Phys.—Usp.*, 2013, vol. 56, no. 7, p. 643.
22. Fojtik, A. and Henglein, A., *Chem. Phys. Lett.*, 1994, vol. 221, p. 363.
23. Kazakevich, P.V., Simakin, A.V., Voronov, V.V., and Shafeev, G.A., *Appl. Surf. Sci.*, 2006, vol. 252, no. 13, p. 4373.
24. Stratakis, E., Barberoglou, M., Fotakis, C., Viau, G., Garcia, C., and Shafeev, G.A., *Opt. Express*, 2009, vol. 17, no. 15, p. 12650.
25. Zhang, Dongshi., Gökce, B., and Barcikowski, S., *Chem. Rev.*, 2017, vol. 117, p. 3990.
26. Xiao, J., Liu, P., Wang, C.X., and Yang, G.W., *Prog. Mater. Sci.*, 2017, vol. 87, p. 140.
27. Shih, C.-Y., Streubel, R., Heberle, J., Letzel, A., Shugaev, M.V., Wu, C., Schmidt, M., Gokce, B., Barcikowski, S., and Zhigilei, L.V., *Nanoscale*, 2018, vol. 10, p. 6900.
28. Povarnitsyn, M.E., Itina, T.E., Levashov, P.R., and Khishchenko, K.V., *Phys. Chem. Chem. Phys.*, 2013, vol. 15, p. 3108.
29. Povarnitsyn, M.E. and Itina, T.E., *Appl. Phys. A*, 2014, vol. 117, no. 1, p. 175.
30. Inogamov, N.A., Zhakhovskii, V.V., and Khokhlov, V.A., *J. Exp. Theor. Phys.*, 2018, vol.127, no. 1, p. 79.
31. Shih Cheng-Yu, Shugaev, M.V., Wu Chengping, and Zhigilei,L.V., *J. Phys. Chem. C*, 2017, vol. 121, no. 30, p. 16549.
32. Petrov, Yu.V., Khokhlov, V.A., Zhakhovsky, V.V., and Inogamov, N.A., *Appl. Surf. Sci.*, 2019, vol. 492, p. 285.
33. Petrov, Yu.V., Inogamov, N.A., Zhakhovsky, V.V., and Khokhlov, V.A., *Contrib. Plasma Phys.*, 2019, vol. 59, no. 6, e201800180.
34. Inogamov, N.A., Khokhlov, V.A., Petrov, Y.V., and Zhakhovsky, V.V., *Opt. Quantum Electron.*, 2020, vol. 52, p. 63.
35. Ionin, A., Ivanova, A., Khmel'nitskii, R., Klevkov, Yu., Kudryashov, S., Mel'nik, N., Nastulyavichus, A., Rudenko, A., Saraeva, I., Smirnov, N., Zayarny, D., Baranov, A., Kirilenko, D., Brunkov, P., and Shakhmin, A., *Appl. Surf. Sci.*, 2018, vol. 436, p. 662.
36. Smirnov, N.A., Kudryashov, S.I., Danilov, P.A., Rudenko, A.A., Ionin, A.A., and Nastulyavichus, A.A., *JETP Lett.*, 2018, vol. 108, no. 6, p.368.
37. Kudryashov, S.I., Danilov, P.A., Porfirev, A.P., Saraeva, I.N., Nguyen, T.N.T., Rudenko, A.A., Khmelnitskii, R.A., Zayarny, D.A., Ionin, A.A., Kuchmizhak, A.A., Khonina, S., and Vitrik, O.B., *Appl. Surf. Sci.*, 2019, vol. 484, p. 948.
38. Kudryashov, S.I., Samokhvalov, A.A., Nastulyavichus, A.A., Saraeva, I.N., Michailovsky, V.Y., Ionin, A.A., and Veiko, V.P., *Materials*, 2019, vol. 12, p. 562.

39. Nastulyavichus, A.A., Kudryashov, S.I., Smirnov, N.A., Rudenko, A.A., Kharin, A.Y., Zayarny, D.A., and Ionin, A.A., *Opt. Laser Technol.*, 2019, vol. 111, p. 75.
40. Kudryashov, S.I., Nastulyavichus, A.A., Ivanova, A.K., Smirnov, N.A., Khmelnitskiy, R.A., Rudenko, A.A., Saraeva, I.N., Tolordava, E.R., Kharin, A.Yu., Zavestovskaya, I.N., Romanova, Yu.M., Zayarny, D.A., and Ionin, A.A., *Appl. Surf. Sci.*, 2019, vol. 470, p. 825.
41. Kruusing, A., *Opt. Lasers Eng.*, 2004, vol. 41, no. 2, p. 307.
42. Peyre, P. Chaieb, I., and Braham,C., *Modell. Simul. Mater. Sci. Eng.*, 2007, vol. 15, no. 3, p. 205.
43. Sano, Y., Masaki, K., Gushi, T., and Sano, T., *Mater. Des. (1980–2015)*, 2012, vol. 36, p. 809.
44. Kolobov, Yu.R., Golosov, E.V., Vershinina, T.N., Zhidkov, M.V., Ionin, A.A., Kudryashov, S.I., Makarov, S.V., Seleznev, S.V., Sinitsyn, D.V., and Ligachev, E.A., *Appl. Phys. A*, 2015, vol. 119, p. 241.
45. Correa, C., Peral, D., Porro, J.A., Diaz, M., Ruiz de Lara, L., Garcia-Beltran, A., and Ocana,J.L., *Opt. Laser Technol.*, 2015, vol. 73, p. 179.
46. Karthik, D. and Swaroop, S., *Mater. Manuf. Processes*, 2017, vol. 32, no. 14, p. 1565.
47. Veiko, V.P., Odintsova, G.V., Gazizova, M.Y., Karlagina, Y.Y., Manokhin, S.S., Yatsuk, R.M., Vasilkov, S.D., and Kolobov, Y.R., *Laser Phys.*, 2018, vol. 28, no. 8, 086002.
48. Trdan, U., Sano, T., Klobcar, D., Sano, Y., Grum, J., and Sturm, R., *Corros. Sci.*, 2018, vol. 143, p. 46.
49. Petrov, Yu.V., Inogamov, N.A., and Migdal, K.P., *JETP Lett.*, 2013, vol. 97, no. 1, p. 20.
50. Petrov, Yu.V. and Inogamov, N.A., *JETP Lett.*, 2013, vol. 98, no. 5, p.278.
51. Milov, I., Lipp, V., Ilnitsky, D., Medvedev, N., Migdal, K., Zhakhovsky, V., Khokhlov, V., Petrov, Yu., Inogamov, N., Semin, S., Kimel, A., Ziaja, B., Makhotkin, I.A., Louis, E., and Bijkerk, F., *Appl. Surf. Sci.*, 2020, vol. 501, 143973.
52. Petrov, Yu., Migdal, K., Inogamov, N., Khokhlov, V., Ilnitsky, D., Milov, I., Medvedev, N., Lipp, V., and Zhakhovsky, V., *Data in Brief*, 2020, vol. 28, 104980.
53. Kudryashov, S.I., Gakovic, B., Danilov, P.A., Petrovic, S.M., Milovanovic, D., Rudenko, A.A., and Ionin, A.A., *Appl. Phys. Lett.*, 2018, vol. 112, no. 2, 023103.
54. Inogamov, N.A. and Petrov, Yu.V., *J. Exp. Theor. Phys.*, 2010, vol. 110, no. 3, p.446.
55. Inogamov, N.A., Zhakhovskii, V.V., Ashitkov, S.I., Khokhlov, V.A., Shepelev, V.V., Komarov, P.S., Ovchinnikov, A.V., Sitnikov, D.S., Petrov, Yu.V., Agranat, M.B., Anisimov, S.I., and Fortov, V.E., *Contrib. Plasma Phys.*, 2011, vol. 51, no. 4, p. 367.
56. Bezhanov, S.G., Kanavin, A.P., and Uryupin, S.A., *Opt. Spectrosc.*, 2013, vol. 114, no. 3, p. 384.
57. Fourment, C., Deneuville, F., Descamps, D., Dorchies, F., Petit, S., Peyrusse, O., Holst, B., and Recoules, V., *Phys. Rev. B: Condens. Matter Mater. Phys.*, 2014, vol. 89, 161110.
58. Bezhanov, S.G., Kanavin, A.P., and Uryupin, S.A., *Quantum Electron.*,2014, vol. 44, no. 9, p. 859.
59. Migdal, K.P., Il'nitsky, D.K., Petrov, Yu.V., and Inogamov, N.A., *J. Phys.: Conf. Ser.*, 2015, vol. 653, 012086.
60. Petrov, Yu.V., Inogamov, N.A., Anisimov, S.I., Migdal, K.P., Khokhlov, V.A., and Khishchenko, K.V., *J. Phys.: Conf. Ser.*, 2015, vol. 653, 012087.
61. Petrov, Yu.V., Migdal, K.P., Inogamov, N.A., and Anisimov, S.I., *JETP Lett.*, 2016, vol. 104, no. 6, p. 431.
62. Petrov, Y.V., Mokshin, A.V., Galimzyanov, B.N., and Inogamov, N.A., *J. Phys.: Conf. Ser.*, 2018, vol. 946, 012096.
63. Migdal, K.P., Zhakhovsky, V.V., Yanilkin, A.V., Petrov, Yu.V., and Inogamov, N.A., *Appl. Surf. Sci.*, 2019, vol. 478, p. 818.
64. Petrov, Yu.V., Inogamov, N.A., Migdal, K.P., Mokshin, A.V., and Galimzyanov, B.N., *J. Phys.: Conf. Ser.*, 2019, vol. 1147, 012069.
65. Migdal, K.P., Petrov, Yu.V., Zhakhovsky, V.V., and Inogamov, N.A., *J. Phys.: Conf. Ser.*, 2019, vol. 1147, 012005.
66. Abrikosov, A.A., *Fundamentals of the Theory of Metals*, Amsterdam: North-Holland, 1988.
67. Peierls, R.E., *Quantum Theory of Solids*, Oxford: Clarendon, 1955.
68. Anisimov, S.I., Kapeliovich, B.L., and Perelman, T.L., *Zh. Eksp. Teor. Fiz.*, 1974, vol. 39, no. 2, p. 375.
69. Ilnitsky, D.K., Khokhlov, V.A., Inogamov, N.A., Zhakhovsky, V.V., Petrov, Yu.V., Khishchenko, K.V., Migdal, K.P., and Anisimov, S.I., *J. Phys.: Conf. Ser.*, 2014, vol. 500, 032021.
70. Khokhlov, V.A., Zhakhovsky, V.V., Khishchenko, K.V., Inogamov, N.A., and Anisimov, S.I., *J. Phys.: Conf. Ser.*, 2016, vol. 774, 012100.
71. Inogamov, N.A., Zhakhovsky, V.V., Khokhlov, V.A., Khishchenko, K.V., Petrov Yu.V., Ilnitsky, D.K., and Migdal, K.P., The role of geometric parameters in femtosecond laser ablation, in*Fiziko-himicheskaya kinetika v gazovoj dinamike* (Physicochemical Kinetics in Gas Dynamics), 2014. www.chemphys.edu.ru/pdf/2014-11-29-005.pdf.
72. Ilnitsky, D.K., Khokhlov, V.A., Zhakhovsky, V.V., Petrov, Yu.V., Migdal, K.P., and Inogamov, N.A., *J. Phys.: Conf. Ser.*, 2016, vol. 774, 012101.
73. Demaske, B.J., Zhakhovsky, V.V., Inogamov, N.A., and Oleynik,I.I., *Phys. Rev. B: Condens. Matter Mater. Phys.*, 2013, vol. 87, 054109.
74. Inogamov, N.A., Zhakhovsky, V.V., Khokhlov, V.A., Demaske, B.J., Khishchenko, K.V., and Oleynik, I.I., *J. Phys.: Conf. Ser.*, 2014, vol. 500, 192023.
75. Hohlfeld, J., Muller, J.G., Wellershoff, S.-S., and Matthias, E., *Appl. Phys. B*, 1997, vol. 64, p. 387.
76. Wellershoff, S.-S., Hohlfeld, J., Gudde, J., and Matthias, E., *Appl. Phys. A*, 1999, vol. 69, no. 1 (suppl.), p. 99.
77. Inogamov, N.A., Zhakhovskii, V.V., and Khokhlov, V.A., *J. Exp. Theor. Phys.*, 2015, vol. 120, no. 1, p. 15.
78. Inogamov, N.A., Zhakhovskii, V.V., Ashitkov, S.I., Khokhlov, V.A., Petrov, Yu.V., Komarov, P.S., Agranat, M.B., Anisimov, S.I., and Nishihara, K., *Appl. Surf. Sci.*, 2009, vol. 255, no. 24, p. 9712.

79. Inogamov, N.A., Petrov, Yu.V., Zhakhovsky, V.V., Khokhlov, V.A., Demaske, B.J., Ashitkov, S.I., Khishchenko, K.V., Migdal, K.P., Agranat, M.B., Anisimov, S.I., Fortov, V.E., and Oleynik, I.I., *AIP Conf. Proc.*, 2012, vol. 1464, p. 593.
80. Ivanov, D.S. and Zhigilei, L.V., *Phys. Rev. B: Condens. Matter Mater. Phys.*, 2003, vol. 68, 064114.
81. Povarnitsyn, M.E., Itina, T.E., Sentis, M., Khishchenko, K.V., and Levashov, P.R., *Phys. Rev. B: Condens. Matter Mater. Phys.*, 2007, vol. 75, 235414.
82. Zhigilei, L.V., Lin Zhibin, and Ivanov, D.S., *J. Phys. Chem. C*, 2009, vol. 113, p. 11892.
83. Inogamov, N.A., Oparin, A.M., Petrov, Yu.V., Shaposhnikov, N.V., Anisimov, S.I., von der Linde, D., and Meyer-ter-Vehn, J., *JETP Lett.*, 1999, vol. 69, no. 4, p.310.
84. Anisimov, S.I., Inogamov, N.A., and Oparin, A.M., *Fluid Dyn.*, 1999, vol. 34, no. 6, p. 896.
85. Zhakhovskii, V.V., Nishikhara, K., Anisimov, S.I., and Inogamov, N.A., *JETP Lett.*, 2000, vol. 71, p.167.
86. Anisimov, S.I., Zhakhovskii, V.V., Inogamov, N.A., Nishikhara, K., Oparin, A.M., and Petrov, Yu.V., *JETP Lett.*, 2003, vol. 77, no. 11, p.606.
87. Sokolowski-Tinten, K., Bialkowski, J., Cavalleri, A., Linde, D., and Oparin, A., *Phys. Rev. Lett.*, 1998, vol. 81, no. 1, p. 224.
88. Temnov, V.V. and Sokolowski-Tinten, K., *J. Opt. Soc. Am. B*, 2006, vol. 23, no. 9, p. 1954.
89. Inogamov, N.A., Zhakhovskii, V.V., Ashitkov, S.I., Petrov, Yu.V., Agranat, M.B., Anisimov, S.I., Nishikhara, K., and Fortov, V.E., *J. Exp. Theor. Phys.*, 2008, vol.107, no. 1, 1.
90. Ashitkov, S.I., Ovchinnikov, A.V., and Agranat, M.B., *AIP Conf. Proc.*, 2012, vol. 1464, no. 1, p. 294.
91. Bonse, J., Bachelier, G., Siegel, J., and Solis, J., *Phys. Rev. B: Condens. Matter Mater. Phys.*, 2006, vol. 74, 134106.
92. Ashitkov, S.I., Komarov, P.S., Ovchinnikov, A.V., Struleva, E.V., and Agranat, M.B., *Quantum Electron.*, 2013, vol. 43, no. 3, p. 242.
93. Bonse, J., Bachelier, G., Siegel, J., Solis, J., and Sturm, H., *J. Appl. Phys.*, 2008, vol. 103, 054910.
94. Hasegawa, N., Nishikino, M., Ishino, M., Ohnishi, N., Ito, A.M., Minami, Y., Baba, M., Faenov, A.Y., Inogamov, N., Kawachi, T., Kondo, K., and Suemoto, T., in *X-Ray Lasers 2016, Proc. 15th Int. Conf. on X-Ray Lasers*, Kawachi, T., Bulanov, S.V., Daido, H., and Kato, Y., Eds., Springer Proceedings in Physics, vol. 202, p. 273.
95. Olbrich, M., Pflug, T., Wustefeld, C., Motylenko, M., Sandfeld, S., Rafaja, D., and Horn, A., *Opt. Lasers Eng.*, 2020, vol. 129, 106067.
96. Winter, J., Rapp, S., Spellauge, M., Eulenkamp, C., Schmidt, M., and Huber, H.P., *Appl. Surf. Sci.*, 2020, vol. 511, 145514.
97. Barker, L.M. and Hollenbach, R.E., *J. Appl. Phys.*, 1972, vol. 43, no. 11, p. 4669.
98. Barker, L.M. and Hollenbach, R.E., *J. Appl. Phys.*, 1974, vol. 45, no. 11, p. 4872.
99. Kanel, G.I., Fortov, V.E., and Razorenov, S.V., *Phys.—Usp.*, 2007, vol. 500, no. 8, p.771.
100. Cai, Y., Wu, H.A., and Luo, S.N., *J. Appl. Phys.*, 2017, vol. 121, 105901.
101. Antoun, T., Seaman, L., Curran, D.R., Kanel, G.I., Razorenov, S.V., and Utkin, A.V., *Spall Fracture (Shock Wave and High Pressure Phenomena)*, New York: Springer, 2003.
102. Kanel, G.I., Razorenov, S.V., and Fortov, V.E., *Shock-Wave Phenomena and the Properties of Condensed Matter*,New York: Springer, 2004.
103. Kanel', G.I.,*Udarnye volny v fizike tverdogo tela* (Shock Waves in Solid State Physics), Moscow: Fizmatlit, 2018.
104. Inogamov, N.A., Anisimov, S.I., and Retfeld, B., *JETP Lett.*, 1999, vol. 88, no. 6, p. 1143.
105. Starikov, S.V. and Pisarev, V.V., *J. Appl. Phys.*, 2015, vol. 117, 135901.
106. Upadhyay, A.K., Inogamov, N.A., Rethfeld, B., and Urbassek, H.M., *Phys. Rev. B: Condens. Matter Mater. Phys.*, 2008, vol. 78, 045437.
107. Zhakhovskii, V.V., Inogamov, N.A., and Nishihara, K., *JETP Lett.*, 2008, vol. 87, p. 423.
108. Zhakhovskii, V.V., Inogamov, N.A., and Nishihara, K., *J. Phys.: Conf. Ser.*, 2008, vol. 112, 042080.
109. Starikov, S.V., Faenov, A.Y., Pikuz, T.A., Skobelev, I.V., Fortov, V.E., Tamotsu, S., Ishino, M., Tanaka, M., Hasegawa, N., Nishikino, M., Kaihori, T., Imazono, T., Kando, M., and Kawachi, T., *Appl. Phys. B*, 2014, vol. 116, p. 1005.
110. Ishino, M., Inogamov, N.A., Tamotsu, S., Zhakhovsky, V.V., Hasegawa, N., Skobelev, I.Yu., Faenov, A.Ya., Pikuz, T.A., Mikami, K., Kawachi, T., and Nishikino, M., *Appl. Phys. A*, 2018, vol. 124, p. 649.
111. Kanel, G.I., Zaretsky, E.B., Razorenov, S.V., Ashitkov, S.I., and Fortov, V.E., *Phys.—Usp.*, 2017, vol. 60, no. 5, p.490.
112. Demaske, B.J., Zhakhovsky, V.V., Inogamov, N.A., and Oleynik, I.I., *Phys. Rev. B: Condens. Matter Mater. Phys.*, 2010, vol. 82, 064113.
113. Ashitkov, S.I., Komarov, P.S., Ovchinnikov, A.V., Struleva, E.V., and Agranat, M.B., *JETP Lett.*, 2016, vol. 103, no. 8, p.544.
114. Struleva, E.V., Ashitkov, S.I., Komarov, P.S., Khishchenko, K.V., and Agranat, M.B., *J. Phys.: Conf. Ser.*, 2016, vol. 774, no. 1, 012098.
115. Ashitkov, S.I., Komarov, P.S., Struleva, E.V., Inogamov, N.A., and Agranat, M.B., *J. Phys.: Conf. Ser.*, 2018, vol. 946, 012002.
116. Struleva, E.V., Komarov, P.S., Yurkevich, A.A., and Ashitkov, S.I., *J. Phys.: Conf. Ser.*, 2019, vol. 1147, 012062.
117. Ashitkov, S.I., Zhakhovsky, V.V., Inogamov, N.A., Komarov, P.S., Agranat, M.B., and Kanel, G.I., *AIP Conf. Proc.*, 2017, vol. 1793.
118. Ashitkov, S.I., Komarov, P.S., Struleva, E.V., Agranat, M.B., and Kanel, G.I., *J. Phys.: Conf. Ser.*, 2019, vol. 1147, 012022.
119. Inogamov, N., Zhakhovsky, V., Ilnitsky, D., and Khokhlov, V., in *Proc. of the 32nd Int. Symp. on Shock Waves (ISSW32)*, Singapore, 2019. https://doi.org/10.3850/978-981-11-2730-4_0506-cd

120. Lasemi, N., Pacher, U., Zhigilei, L.V., Bomati-Miguel, O., Lahoz, R., and Kautek, W., *Appl. Surf. Sci.*, 2018, vol. 433, p. 772.
121. Inogamov, N., Ashitkov, S., Zhakhovsky, V., Shepelev, V., Khokhlov, V., Komarov, P., Agranat, M., Anisimov, S., and Fortov, V., *Appl. Phys. A*, 2010, vol. 101, no. 1, p. 1.
122. Agranat, M.B., Anisimov, S.I., Ashitkov, S.I., Zhakhovskii, V.V., Inogamov, N.A., Komarov, P.S., Ovchinnikov, A.V., Fortov, V.E., Khokhlov, V.A., and Shepelev, V.V., *JETP Lett.*, 2010, vol. 91, no. 9, p.471.
123. Inogamov, N.A., Zhakhovsky, V.V., Ashitkov, S.I., Agranat, M.B., Komarov, P.S., Khokhlov, V.A., and Shepelev, V.V., *AIP Conf. Proc.*, 2010, vol. 1278, p. 590.
124. Karim, E.T., Shugaev, M.V., Wu, C., Lin, Z., Matsumoto, H., Conneran, M., Kleinert, J., Hainsey, R.F., and Zhigilei, L.V., *Appl. Phys. A*, 2016, vol. 122, p. 407.
125. Shugaev, M.V., Shih, C.-Y., Karim, E.T., Wu, C., and Zhigilei, L.V., *Appl. Surf. Sci.*, 2017, vol. 417, p. 54.
126. Inogamov, N.A., Khokhlov, V.A., and Zhakhovskii, V.V., *JETP Lett.*, 2018, vol. 108, no. 7, p. 439.
127. Li, Q., Alloncle, A.P., Grojo, D., and Delaporte, F., *Appl. Phys. A*, 2017, vol. 123, p. 718.
128. Li, Q., Alloncle, A.P., Grojo, D., and Delaporte, F., *Opt. Express*, 2017, vol. 25, no. 20, p. 24164.
129. Li, Q., Grojo, D., Alloncle, A.P., and Delaporte, F., *Appl. Surf. Sci.*, 2019, vol. 471, p. 627.
130. Li, Q., Grojo, D., Alloncle, A.P., and Delaporte, F., *Opt. Mater. Express*, 2019, vol. 9, no. 8, p. 3476.
131. Veiko, V.P., Volkov, S.A., Zakoldaev, R.A., Sergeev, M.M., Samokhvalov, A.A., Kostyuk, G.K., and Milyaev, K.A., *Quantum Electron.*, 2017, vol. 47, no. 9, p. 842.
132. Tsvetkov, M.Yu., Minaev, N.V., Akovantseva, A.A., Timashev, P.S., Muslimov, A.E., and Kanevskii, V.M., *Quantum Electron.*, 2019, vol. 49, no. 2, p. 133.
133. Mirza, I., Bulgakova, N.M., Tomášťík, J., Michálek, V., Haderka, O., Fekete, L., and Mocek, T., *Sci. Rep.*, 2016, vol. 6, p. 39133.
134. Ravi-Kumar, S., Lies, B., Lyu, H., and Quin, H., *Procedia Manuf.*, 2019, vol. 34, p. 316.
135. Fabbro, R., Fournier, J., Ballard, P., Devaux, D., and Virmont, J., *J. Appl. Phys.*, 1990, vol. 68, no. 2, p. 775.
136. Inogamov, N.A., Dem'yanov, A.Yu., and Son, E.E., *Gidrodinamika peremeshivaniya: Periodicheskie struktury, usilenie subgarmonik, inversnyi kaskad* (Mixing Hydrodynamics: Periodic Structures, Amplification of Subharmonics, Inverse Cascade), Moscow: Mosk. Fiz.-Tekh. Inst., 1999.
137. Inogamov, N.A., *Astrophys. Space Phys. Rev.*, 1999, vol. 10, part 2, p. 1.
138. Dyachkov, S.A., Zhakhovsky, V.V., Parshikov, A.N., and Inogamov, N.A., *J. Phys.: Conf. Ser.*, 2019, vol. 1147, 012064.
139. Inogamov, N.A., Zhakhovsky, V.V., and Khokhlov, V.A., *J. Phys.: Conf. Ser.*, 2018, vol. 946, 012008.
140. Ivanov, D.S., Blumenstein, A., Ihlemann, J., Simon, P., Garcia, M.E., and Rethfeld, B., *Appl. Phys. A*, 2017, vol. 123, p. 744.
141. Saraeva, I.N., Kudryashov, S.I., Rudenko, A.A., Zhilnikova, M.I., Ivanov, D.S., Zayarny, D.A., Simakin, A.V., Ionin, A., and Garcia, M.E., *Appl. Surf. Sci.*, 2019, vol. 470, p. 1018.

Translated by A. Sin'kov